Automatic image acquisition, calibration and montage assembly for biological X-ray microscopy

B. W. LOO JR*, W. MEYER-ILSE† & S. S. ROTHMAN‡

Bioengineering Graduate Group, University of California, San Francisco and Berkeley, School of Medicine, University of California, Davis, California, U.S.A.

†*Center for X-Ray Optics, Ernest O. Lawrence Berkeley National Laboratory, MS 2-400, Berkeley, CA 94720, U.S.A.*

‡*Departments of Physiology and Stomatology, University of California, 513 Parnassus Avenue, Box 0444, San Francisco, CA 94143, U.S.A.*

Summary

We describe a system for the automatic acquisition and processing of digital images in a high-resolution X-ray microscope, including the formation of large-field high-resolution image montages. A computer-controlled sample positioning stage provides approximate coordinates for each high-resolution subimage. Individual subimages are corrected to compensate for time-varying, non-uniform illumination and CCD-related artefacts. They are then automatically assembled into a montage. The montage assembly algorithm is designed to use the overlap between each subimage and multiple neighbours to improve the performance of the registration step and the fidelity of the result. This is accomplished by explicit use of recorded stage positions, optimized ordering of subimage insertion, and registration of subimages to the developing montage. Using this procedure registration errors are below the resolution limit of the microscope (43 nm). The image produced is a seamless, large-field montage at full resolution, assembled automatically without human intervention. Beyond this, it is also an accurate X-ray transmission map that allows the quantitative measurement of anatomical and chemical features of the sample. Applying these tools to a biological problem, we have conducted the largest X-ray microscopical study to date.

Correspondence to: Billy W. Loo Jr, Genteric Corporation, 2061 Challenger Drive, Alameda, CA 94501, U.S.A. E-mail: BWLoo@lbl.gov

Introduction

X-ray microscopy has some unique and attractive features as a tool for biological imaging (Schmahl *et al.*, 1980; Rothman *et al.*, 1990; Kirz *et al.*, 1995). Among the most important are high contrast due to the natural constituent molecules in cells and tissues, and significantly higher resolution than visible light microscopy. In an X-ray microscope, low energy X-rays (with wavelengths ranging from 2 to 4 nm in this work) illuminate a sample, and an image is formed from the transmitted photons. Materials absorb these 'soft' X-rays in a manner highly dependent on their elemental and chemical composition (Henke *et al.*, 1993). This 'natural contrast' permits quantitative measurement of the distribution of intrinsic cellular components (e.g. carbon, nitrogen, protein, DNA) without stains. In addition, the relatively high penetration of soft X-rays (up to several micrometres) allows imaging of a wide range of samples from standard embedded tissue sections of various thickness to whole cells in their native state (e.g. in aqueous media). High-resolution imaging is made possible by microfabricated diffractive optical elements that are used as lenses, called zone plates (Anderson & Kern, 1992; Schmahl *et al.*, 1996), whose fine feature size allows imaging with 43 nm resolution in the microscope used here (Heck *et al.*, 1999). This is five times the maximum resolution of a standard visible light microscope.

In recent years, the development of high quality zone plate lenses as well as the availability of high brightness sources of X-rays, in the form of synchrotron radiation facilities, has allowed the building of a number of practical

X-ray microscopes (Thieme *et al.*, 1998) that are only now beginning to yield biological results. At this early stage, much work is needed to make the X-ray microscope a useful tool for routine research in biology and to exploit its features fully. To achieve this goal, development is required in three areas: microscope instrumentation, sample preparation, and digital image acquisition and processing. This paper deals primarily with the last of these. In it we describe how we acquire image data and obtain accurate quantitative information from them, and how we extend the high resolution of the method over large fields of view. As a practical matter, the methods must be automatic to allow for the processing of large numbers of samples encompassing large fields of view.

Quantitative imaging requires characterizing the properties and inherent sources of error of each component of the microscope system. Two in particular concern us here. The synchrotron source has a time-varying intensity and pattern of illumination for which we must compensate, and the charge-coupled device (CCD) camera used for image recording introduces artefacts, such as dark current and non-uniform pixel response. Although methods for correcting CCD-related artefacts are standard and well documented in the literature (e.g. Krivanek & Mooney, 1993), here we describe our particular approach and the issues specific to our system.

To take advantage of the high resolution of the X-ray microscope, we must use high magnification and consequently sacrifice field of view. This trade-off is found in almost all forms of microscopy, regardless of the wavelength of illumination (electrons, X-rays or visible light), particularly in full-field imaging. This applies even to many forms of scanning microscopy, as scanning stages often have a smaller range of motion as the step size becomes finer. As a result, it has been difficult to undertake projects that require sampling large areas at high resolution, for example studying samples with both small and large scale features, or survey and screening studies. One solution to this problem is to build large-field composite images from many smaller high-resolution subimages, a process variously referred to as montaging, mosaicking, field stitching or tiling. Automatic montage assembly for various kinds of photography and videography has been developed extensively in computer vision and graphics (e.g. Dani & Chaudhuri, 1995; Davis, 1998). Similar methods have been applied to microscopic imaging, including the assembly of huge montages in electron microscopy (Vogt *et al.*, 1996), and three-dimensional montages in visible light microscopy (Turner *et al.*, 1997). A number of commercial implementations are also available. Below we describe the system we have designed for automatically acquiring digital images and assembling large-field montages of arbitrary size at the full resolution of the X-ray microscope and we demonstrate its application to biological samples.

Methods

The X-ray microscope

We used a digital X-ray microscope, called XM-1 (Meyer-Ilse *et al.*, 1995, 1998), at the Advanced Light Source (ALS) synchrotron radiation facility at Lawrence Berkeley National Laboratory (LBNL). XM-1 is a conventional-type, or full-field imaging, transmission microscope. A condenser zone plate demagnifies the incoherent light source (a bending magnet on the ALS) onto the sample, and an objective zone plate images the sample onto an image detector. Two components of the microscope, the image detector and the sample stage, have a particular impact on calibrating images and assembling large-field montages.

The image detector is a CCD camera, thinned and back-illuminated for high efficiency detection of soft X-rays (Wilhein *et al.*, 1994). The CCD chip has a 1024×1024 array of $24\,\mu m$ pixels. The field of view of XM-1 in its most heavily used configuration is a circular area approximately $10\,\mu m$ in diameter, and at $2400 \times$ magnification (the one most often used) this field, projected to the image plane, matches the width of the CCD. The corresponding pixel size in the image is $10\,nm$. Often, we use subsampling by binning CCD pixels together to reduce the exposure time and data storage requirements. At 2 times binning, or a $20\,nm$ pixel size, the Nyquist sampling criterion is still met for $40\,nm$ resolution. When total field size is a more important consideration than raw resolution, 4 times binning can be used. The digital data from the CCD are read directly into a computer, which facilitates subsequent processing.

The sample positioning system, developed at LBNL, has a unique design, with two separate sample stages, one each in the X-ray microscope (XM), and an external visible light microscope (VLM). Stage position readout is accomplished using Heidenhain optical encoder scales in three orthogonal directions on each stage, with readout increments of $20\,nm$. A magnetic kinematic mounting system allows mounting and unmounting of the sample on and off a stage with a reproducibility comparable to the resolution of the microscope, in the tens of nanometres. The three-dimensional coordinate systems of the two stages are related to each other by a matrix transformation incorporating the relative offset, rotation, and skew between them. The correspondence between positions in the two stages is accurate to less than $2\,\mu m$ in the object plane, and about $1\,\mu m$ along the optical axis, or approximately the depth of focus of both the VLM (with a $0\cdot6\,NA$ objective lens) and the XM. Thus, using this system it is possible to select and focus on sample areas of interest entirely within the VLM. Sample exposure to X-rays is thereby limited to the final image recording, minimizing dose. This is a critical consideration for dose-sensitive samples. The sample stage coordinates at which

each image is acquired are recorded and saved with the image data, and then used in the montage assembly process as estimates of subimage position.

Acquisition of high-resolution subimages in XM-1

When acquiring subimages for montage assembly, the centre and total width of the area of interest are recorded using the graphical interface of the microscope control software. A rectangular grid of equally spaced subimage positions is then computed to cover the region. For circular subimage fields, this pattern of coverage is not ideal, because in order to have sufficient overlap between neighbouring subimages along the diagonals, there is more overlap than necessary between horizontal and vertical neighbours. An equidistant triangular pattern of coverage would be optimal, and should be relatively easy to implement. The grid spacing is typically between 5 and 6 μm, depending on the subimage field diameter (usually about 8 μm), giving 0·5–2 μm (or 25–100 pixels in the case of 2 times binning) of maximum overlap between neighbouring subimages.

Under computer control, the sample stage is sequentially moved to each of the preselected subimage positions and the sample is exposed. The current in the synchrotron storage ring continuously decreases with time, resulting in decreased source intensity. Thus, when acquiring each subimage, the ring current is read, and exposure time adjusted automatically to compensate. The exposure, or product of ring current and exposure time measured in milliampere-seconds (mAs), is kept approximately constant across all subimages. At regular intervals in the subimage acquisition sequence, preselected empty areas on the sample window containing no sample features are exposed to provide background images to be used for field inhomogeneity correction (described below). The entire process, except for user selection of the region of interest and background areas, and the initial selection of the exposure level, is automated.

Corrections applied to individual subimages

1. Dark current correction. The major sources of signal in the CCD camera are charge generated by image-forming X-ray photons, and dark current. Dark current in a CCD pixel is due to the accumulation of thermally generated charge carriers over the integration time, and is highly dependent on temperature (Dereniak & Crowe, 1984). The temperature of the CCD chip is maintained at −50 °C by a thermoelectric cooler to keep dark current at an acceptable level. We modelled dark current signal in each pixel as an affine linear function of integration (exposure) time that is additive to the photon-produced signal. In addition, there is an intensity offset that is added to the signal by the camera

readout electronics to prevent readout noise from generating negative intensity values.

Dark current images are collected for camera calibration on a periodic basis by acquiring images with no light on the camera. Multiple dark current images are acquired at each of several different exposure times and several different camera binning factors. Linear regression is performed on a pixel by pixel basis, giving a slope and offset of dark current versus exposure time for each pixel. Most of the offset component is due to the above-mentioned intensity baseline offset. Figure 1a is an image of the dark current slope in the CCD camera. From these measurements, 'bad' pixels are identified. These are pixels that saturate due to dark current within a specified exposure time, or have slope or offset different from the mean of the array by more than a specified tolerance (typically 10 standard deviations), or are unresponsive as demonstrated by a zero variance over multiple exposures. Between 0·4 and 0·9% of the image pixels are bad, depending on the binning factor, with the higher proportion occurring with more binning. The dark current slope and offset, and the bad pixels, are recorded in a calibration file for each binning factor.

Each subimage is corrected for dark current by subtracting a corresponding calculated dark current image, i.e. the offset plus the slope times the exposure time of the subimage. This is in principle a photometrically accurate correction. This is different from the standard procedure of subtracting a single acquired dark image with the same exposure time as the subimage, and has the theoretical advantage that it does not add the small amount of noise due to statistical variations in dark current signal and readout noise.

To illustrate the small magnitude of the dark current contribution, the signal intensity due to X-ray photons in a background image that is saturated to about 60% of the camera's dynamic range in about 12 s (Fig. 1b) is approximately 1200 times greater than the dark current signal in that exposure time. A significant increase in dark current was noted once, which led to the discovery that the CCD chip had lost contact with the thermoelectric cooler. The problem resolved as soon as this was corrected. We have also noted a very slow but measurable increase in dark current with X-ray exposure over the lifetime of the instrument, presumably due to radiation damage. This can be seen to some extent in Fig. 1a in the pattern of dark current slope, as some parts of the chip were much more heavily exposed than others during the initial alignment of optical components in the microscope.

2. Region of support selection and exposure normalization. The field of view in each subimage is circular and therefore does not fill the entire square CCD pixel array. An iris in front of the camera is used to block off areas outside the field of view, and can be adjusted to exclude scattered
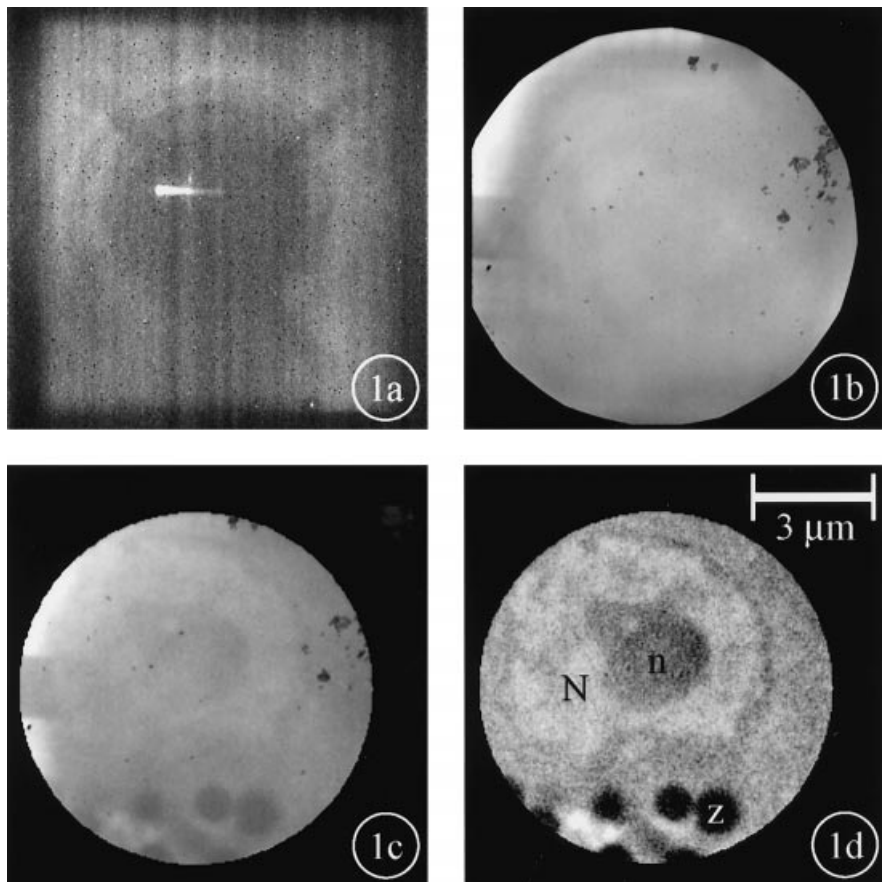
Fig. 1. Corrections applied to individual subimages. a, An image of CCD dark current slope. Some areas of the chip accumulate dark current signal faster than others, possibly due to radiation damage from heavy hard X-ray exposure during the initial alignment of microscope optics. b, A background image obtained by exposing a sample-free area of the sample holder, demonstrating inhomogeneous intensity due to nonuniformity in illumination and pixel sensitivity. c, An uncorrected subimage of part of a pancreatic acinar cell. The region of support, or information-containing area, of the image has been identified, and pixels outside this region have been set to a value of zero. d, The corrected subimage, after subtraction of dark current signal and normalization to the background image. The background response is now uniform, and true sample features are clearly seen, including the cell nucleus (N) and nucleolus (n), and several zymogen granules (z).

light that is more intense at the periphery of the field. The information-containing area of the images, or region of support, which is the same for all images with the same camera iris setting, is identified interactively. The remainder of the pixels are masked off by setting them to a value of zero (see Fig. 1c). A typical region of support has a diameter of about 8 μm in the sample plane.

As described above, the exposure time is adjusted automatically to compensate for decreasing beam intensity over time. Any remaining differences in exposure between subimages are balanced by dividing each subimage by its measured exposure (in mAs).

3. Field inhomogeneity correction. The image field may be inhomogeneous because of non-uniform illumination and non-uniform pixel response or sensitivity to light. Both factors cause differing rates of signal accumulation between pixels and cannot be isolated from each other. However, we can simultaneously compensate for all sources of inhomogeneity that cause such a multiplicative effect by dividing each sample image by a background image. Additive phenomena, such as scattered light that reaches the camera, are not properly corrected by this means. A background image is an image of an area on the sample holder that contains no sample features. In a perfect system,

such an image should have uniform intensity across the field. Any inhomogeneity is due to artefacts. Figure 1b shows a background image acquired in XM-1. Some of the patterns on the image are due to debris or dirt on the CCD camera that obstruct some pixels and thereby decrease their sensitivity to X-rays by absorbing part of the signal.

If the pattern of illumination were constant with time, it would be possible to use the standard procedure of normalizing all images to a single background image formed by averaging several exposures with no sample in the beam. However, we have found that during the course of a long subimage acquisition sequence, the background pattern changes smoothly with time, possibly due to a drift in the position of the ALS beam or components in the optical path (see Fig. 5). Therefore, background images must be acquired at multiple time points throughout the subimage acquisition sequence. At each of these times, several empty areas on the sample window are imaged. They are averaged together to reduce the effect of photon shot noise, and the effect of dirt or other features that are inadvertently captured within any of the background images. To minimize further the effect of extraneous features, the sample stage is moved to an out-of-focus plane to blur them. Finally, if any noticeable effects due to blemishes in the background image

remain, the pixels can be identified interactively and replaced by the average of the corresponding pixels from the other background images acquired at the same time.

Because background images are collected throughout the subimage collection sequence, each subimage is bracketed in time by two background images. The acquisition time of every subimage and background image is recorded with the image data. This allows the generation of a time interpolated background image for each subimage, by performing a pixel by pixel linear interpolation between the bracketing background images.

Each background image is subjected to the same dark current correction, region of support masking, and exposure normalization as described for the individual subimages. Each subimage is then corrected by division by its corresponding background image. As seen in Fig. 1d, the corrected image shows only the true sample structure, with a homogeneous background response. Despite these corrections, we occasionally found a small amount of additional intensity, particularly near the edges of the field of view, probably due to an additive signal such as scattered light in the microscope system. This is usually only noticeable in an assembled montage, where it appears as a small intensity mismatch at the borders of neighbouring subimages (see Fig. 6).

Assembling subimages into a large-field montage

After the individual subimages are corrected, they are inserted into the montage. The goal is to register each subimage accurately with the target region in the montage into which it is to be inserted. We assume that magnification and rotation are constant over all subimages, and that registration can be accomplished solely by translation. As shown, the quality of the resulting registration reinforces the validity of this assumption in our system. The ability to register any two images with one another improves as the feature overlap between them increases. The montage assembly algorithm attempts to maximize feature overlap between any subimage and its target area in the montage. The recorded sample stage positions are used at multiple steps in the process.

First, a subimage adjacency table is generated, identifying which subimages neighbour which, based on their stage positions and the subimage field size defined by the region of support mask, as described above. The dimensions of the entire montage are similarly calculated, and the subimage closest to the centre of the field is identified. Starting with the centremost subimage, an optimized insertion order is determined as follows: the adjacency table is used to organize subimages into sequential generations of neighbours, the first generation being the immediate neighbours of the centremost subimage, the next being their neighbours, and so on. Subimages within each generation are

sorted in order of their distance from the centremost subimage, again based on their stage positions.

Next, an empty image array is created with the dimensions of the full montage, with a small margin added to accommodate possible errors in the stage positions. A correspondence is calculated between the pixel positions in the montage and the stage positions. The centremost subimage is then inserted into the appropriate position in the montage. As each subsequent subimage is inserted, the correspondence between pixel and stage positions allows identification of the target area of the developing montage into which it will be inserted. This target area contains contributions from the parts of previously inserted subimages that overlap with the current one. It is extracted from the montage, and used as a reference image to which the current subimage is registered. The amount of translation or shift that must be applied to the subimage to register it to the reference region is calculated. The subimage is then inserted into the montage at a position appropriately shifted relative to its corresponding stage position.

This approach has a number of advantages. It saves on computation because each subimage is registered only once (with a corresponding reference region from the developing montage) rather than pairwise with each of its neighbours. Also, because reference regions contain data from more than one previously registered subimage, there is much more feature overlap with the subimage to be inserted than there would be if registration were performed pairwise between individual subimages. Figure 2a shows a subimage, and the reference region from the developing montage to which it is registered.

The registration step itself is a form of generalized correlation operation (Knapp & Carter, 1976; Azaria & Hertz, 1984) with the addition of a non-linear processing step. The non-linear processing step, a gradient magnitude operation, is performed first on the subimage and its reference image. This highlights the features in the images, producing a bright signal at object edges, and a dark signal in the relatively uniform areas in the background and in the interior of objects. Figure 2b shows the gradient magnitude images of the subimage and reference image in Fig. 2a. The result is a sharpening of the peak produced by the subsequent correlation step (Fig. 2 insets). We used a Sobel gradient operator, which performs well in the presence of typical noise levels, to compute the gradients of each subimage and its reference image.

A filtered cross-correlation operation is then performed on the gradient magnitude images to determine by what amount the subimage should be shifted relative to its reference image and therefore its recorded stage position. Each cross-correlation is computed over a range of shifts corresponding to zero plus and minus $0.6\,\mu$m with respect to the stage position for the subimage being inserted. This
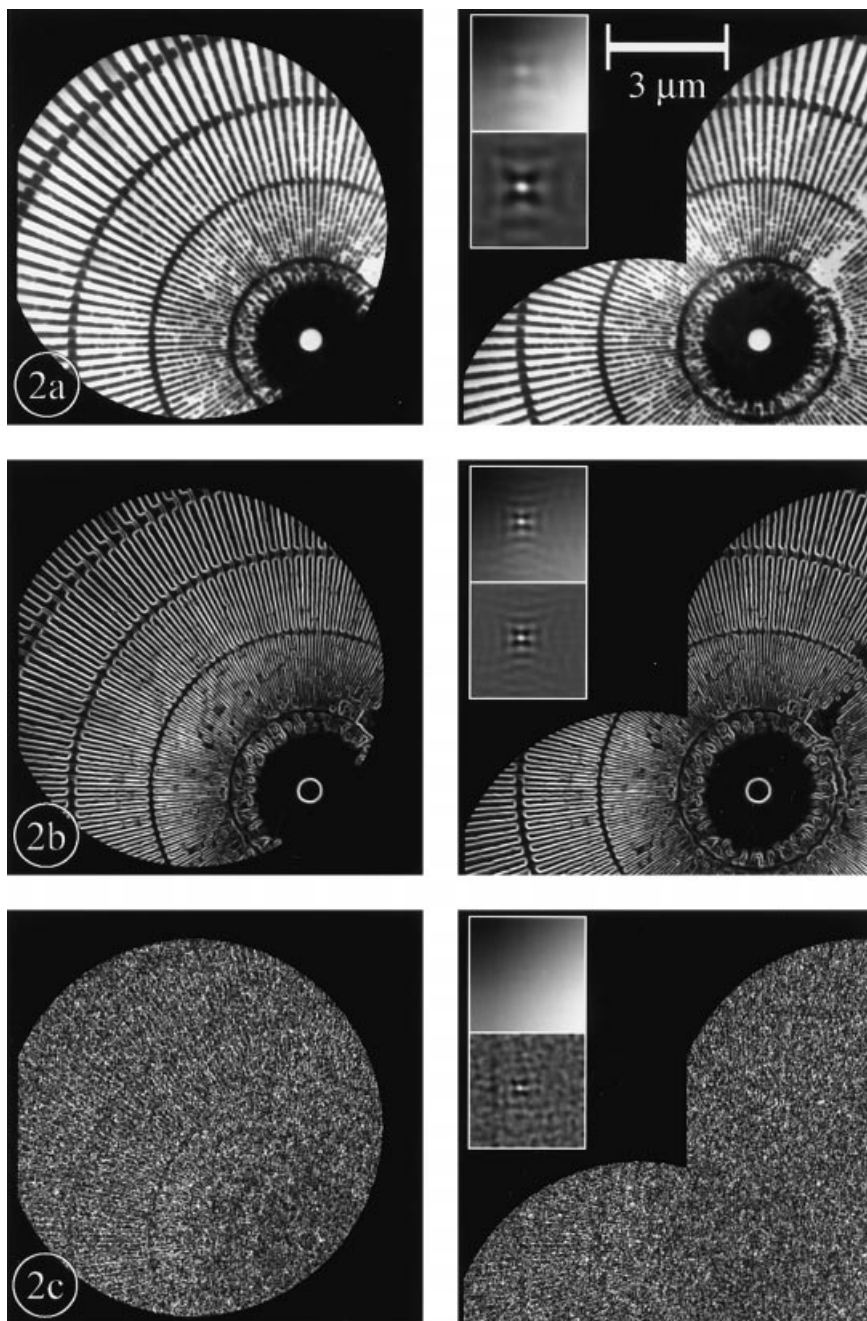
Fig. 2. Subimage registration. As each sub-image (a, left) is inserted into the montage, it is registered with respect to a reference image extracted from its target area in the developing montage (a, right). The reference image contains contributions from more than one previously inserted sub-image, increasing feature overlap and the performance of the registration. The registration step itself is a filtered cross-correlation operation applied to the gradient magnitude images (b) of the subimage and its reference image. The inset images show the results of cross-correlation between each of the subimage/reference pairs. Using the gradient magnitude operation results in a significantly sharper correlation peak. The top of each inset pair is the direct cross-correlation, while the bottom is the filtered cross-correlation. Filtering enhances the peak and suppresses the slowly varying intensity background caused by the small amount of overlap between the images. c, The same as b, but with a large amount of artificial noise added to the source images. Despite the significant degradation of the gradient magnitude images, the correlation peak is still distinct and its position is unchanged.

accommodates the largest anticipated shift based on the accuracy of stage position readout, plus a safety margin. A difference of Gaussians bandpass filter is applied to the cross-correlation image to sharpen peaks while suppressing noise. The position of the highest peak in the filtered cross-correlation image is used to determine the shift to apply. Figure 2c demonstrates that the peak position is unaffected by the addition of a substantial amount of artificial Gaussian noise. In this example, the standard deviation of the noise was chosen to be two-thirds the difference in intensity between the bars and spaces of the test structure

(signal-to-noise ratio, SNR, of 1·5), far more than typical for this kind of imaging.

The subimage is then inserted into the montage at its shifted coordinates. Figure 3a shows a registered set of gradient magnitude subimages. Their corresponding cross-correlation images are in Fig. 3b. While all the cross-correlation images are scaled to comparable brightness in the display, the range of the peak correlation intensities spans nearly four orders of magnitude. With very few exceptions, even at the lowest end of the range, the peaks are prominent enough to identify the appropriate shift uniquely.

Each pixel value in the areas of overlap between adjacent subimages is computed as the average of all the subimage pixels contributing to it. This increases the SNR in the areas of overlap and minimizes wasted radiation exposure to any part of the sample in the sense that all of the exposure goes towards improving image quality. A completed montage of thin gold structures used as high-resolution test objects is in Fig. 4c.

Finally, as mentioned above, despite all the corrections there is occasionally a noticeable intensity mismatch in the montage at subimage borders, due to some uncorrected factor such as scattered light. Without knowing the nature of the source of the artefact, it is not possible to correct for it. However, its appearance can be minimized by blending subimages into the mosaic. Rather than doing a straight average in the overlapping areas, a weighted average is used, with the weights for each subimage tapering smoothly to zero near its border. Figure 6 shows the effect of this blending. This is, of course, not a true correction, but still it is helpful in minimizing the impact of the artefact on subsequent image analysis or processing, such as automated image segmentation (Loo *et al.*, 1996).

Results

Microfabricated resolution test objects

We evaluated the performance of our image acquisition and processing system on real microscope images taken of two thin gold structures microfabricated for the purpose of testing microscope resolution. The two structures, each with a diameter of $47 \mu m$, together spanning a region $94 \mu m$ across, have features down to approximately 40 nm in dimension. Figure 4c is a montage of the full field of view containing both test structures, a composite of 200 subimages. The insets are magnified views of the central portions containing the finest features, demonstrating the full resolution of the microscope. The pixel size is 20 nm.

The performance of the registration can be assessed by comparing high-detail areas in the montage to the original subimages containing the same features. Figure 4a shows two original subimages from the central regions of the test structures. No degradation in resolution is discernible in the corresponding areas of the montage, despite overlap from several subimages, indicating registration errors smaller than the resolution limit of the microscope. In addition, as mentioned above, the corresponding montage areas have better SNR because of the contribution of signal from multiple subimages.

Because of the montage assembly algorithm's essentially perfect registration performance, at least on high contrast structures such as the resolution test objects, we found that it could be used to aid in a number of microscope diagnostics. In comparing the recorded stage positions of the subimages of the test objects to their adjusted positions,

we found a non-random pattern of discrepancy. These were determined to be due to a $1 \cdot 8\%$ error in the microscope magnification, corresponding to a $2 \cdot 8$ cm error in the sample-to-CCD distance (over a total of $1 \cdot 56$ m), and a $0 \cdot 39°$ rotation between the CCD camera and the sample stage. No skew between the sample stage axes was identified. These errors are easily compensated for by a simple matrix transformation. A small random mismatch remained due to the limited precision of the optical encoder readout. Initially, we found the mean error in the determination of position to be substantially worse than expected based on the manufacturer's specified tolerance of 30 nm in the encoder readout. The problem was traced at least in part to an incorrect voltage offset in the optical encoders. After correction of this problem, the mean position determination error, or the distance between each recorded stage position of a subimage and its true position, was 90 nm with a standard deviation of 50 nm. However, because the direction of the error is random, the mutual misregistration between any two adjacent subimages is somewhat larger at about 110 nm on average, with a standard deviation of 60 nm, sufficient to cause substantial degradation of the resolution without correction as seen in Fig. 4b. This information can be used to set a limit on the maximum shift to calculate in the registration step.

Biological samples

Applying the techniques to a biological problem (Rothman *et al.*, 1992; Loo *et al.*, 1996), we set out to measure the population statistics on the size, protein mass and number of zymogen granules in pancreatic exocrine tissue. A quantitative morphometry problem such as this requires measurement of large samples to obtain a statistically meaningful estimate of these population parameters. In addition, it requires imaging large fields of view, because zymogen granules are distributed very unevenly, usually being clustered around ductal structures in the tissue.

Figure 7 is a montage of 400 subimages of a plastic embedded tissue section of rat pancreas, nominally $0 \cdot 75 \mu m$ thick. The sample is unstained, and at the imaging wavelength used ($2 \cdot 4$ nm) the contrast in such a plastic embedded sample is based primarily on the nitrogen content of the tissue, effectively providing a density map of protein and nucleic acid. The total field of view is $110 \mu m$ across, or about 2700×2700 pixels at 40 nm pixel size. The pancreatic cells are arranged in cluster-like units called acini, surrounding a duct system that conveys secreted material eventually to the gut. At their apical end, adjacent to the duct, the cells are packed with dense, sphere-like zymogen granules. Supporting structures are seen, such as red blood cell carrying capillaries, as are other intracellular organelles, such as mitochondria. The magnified view in Fig. 7b demonstrates additional fine structure, including
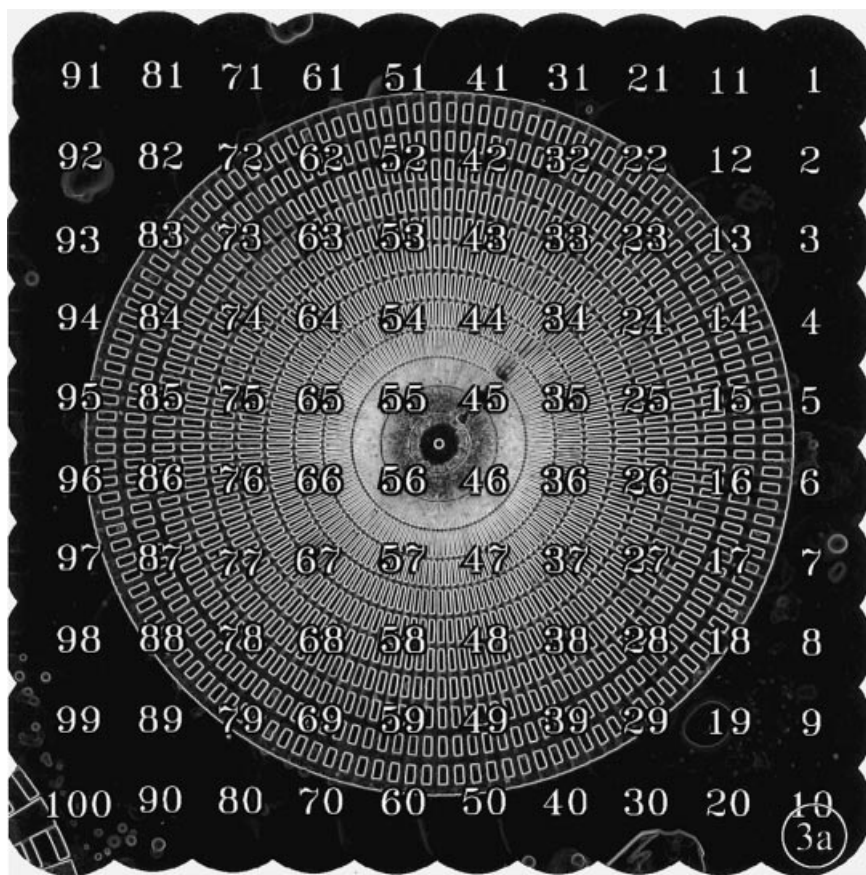
Fig. 3. Cross-correlation registration. a, A set of registered gradient magnitude images. The numbers indicate the temporal order of subimage acquisition. b, The corresponding cross-correlation arrays between subimages and their reference images, in order of insertion sequence. Subimage 46, the centremost subimage, was inserted first (so cross-correlation is not performed on it). It is followed by the rest in an optimized sequence determined by the montage assembly algorithm. The position of the cross-correlation peak indicates the amount of shift required for proper registration. The crosses indicate the origin of the cross-correlation arrays, corresponding to zero shift. Subimages 11 and 90 have almost featureless areas of overlap with subimages inserted before them, and therefore have ambiguous cross-correlation peaks. However, subimages with even minimal features in their overlap areas (e.g. 1, 2, 10, 81 and 91) still have distinct peaks, demonstrating the robustness of the method. The range of the peak intensities shown here spans nearly four orders of magnitude.

patterns of linear lucencies well beyond the ability of visible light microscopes to resolve. These may represent endoplasmic reticulum cisternae orientated perpendicular to the plane of sectioning, but whatever their identity they indicate the high resolution of the method.

The zymogen granules, often under 1μm in size, are beyond the ability of the standard visible light microscope to measure and count accurately. Nor is there a direct way to quantify their protein content in either the visible light or electron microscopes. With its combination of high resolution and natural contrast, X-ray microscopy, in particular, large-field X-ray microscopy, can make all of the desired measurements on zymogen granules (size, number, and protein content) and is to the best of our knowledge the only tool available at present to do so. Nearly 100 such montages were assembled in this study, requiring the acquisition of nearly 27 000 subimages, making it the largest X-ray microscopical study to date. The biological results will be published in a separate paper.

Discussion

We have developed digital imaging methods to help realize and enhance key strengths of X-ray microscopy, in particular high natural contrast permitting quantitative

measurements, and high resolution. Quantitative X-ray imaging can only be accomplished by accounting for and correcting several instrument-related sources of error. To this end we have characterized the components of our system and shown how photometrically accurate images can be produced. We have also developed a method for acquiring images that retains the high resolution of X-ray microscopy while allowing an arbitrarily large field of view.

Although parts are similar to methods found in the literature, the montage assembly algorithm presented has a number of distinguishing features. In particular, it makes explicit use of recorded sample stage positions to estimate the overall size of the montage field and the distance between subimages, to generate a subimage adjacency table, to compute coordinates for extracting target regions from the developing montage, and to calculate the required size of the cross-correlation arrays. It also determines an optimized subimage insertion order based on the adjacency table and the distance of subimages from the centre of the developing montage. These two features provide dependable performance with arbitrary subimage acquisition order and adjacency pattern. That is to say, no assumptions are required about the spatial or temporal organization of the subimages. The algorithm will assemble the montage from all subimages that have a pathway of connectivity with a
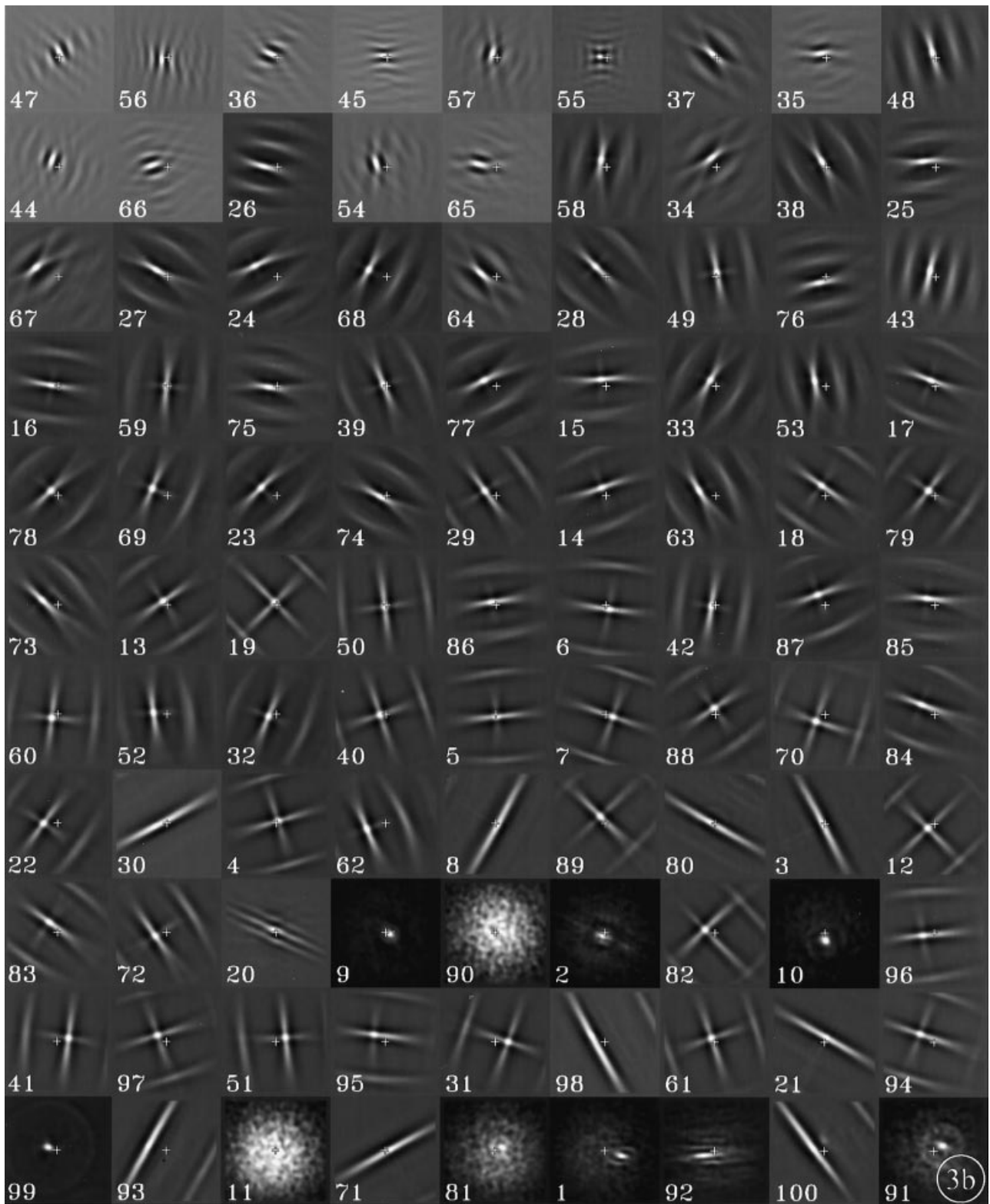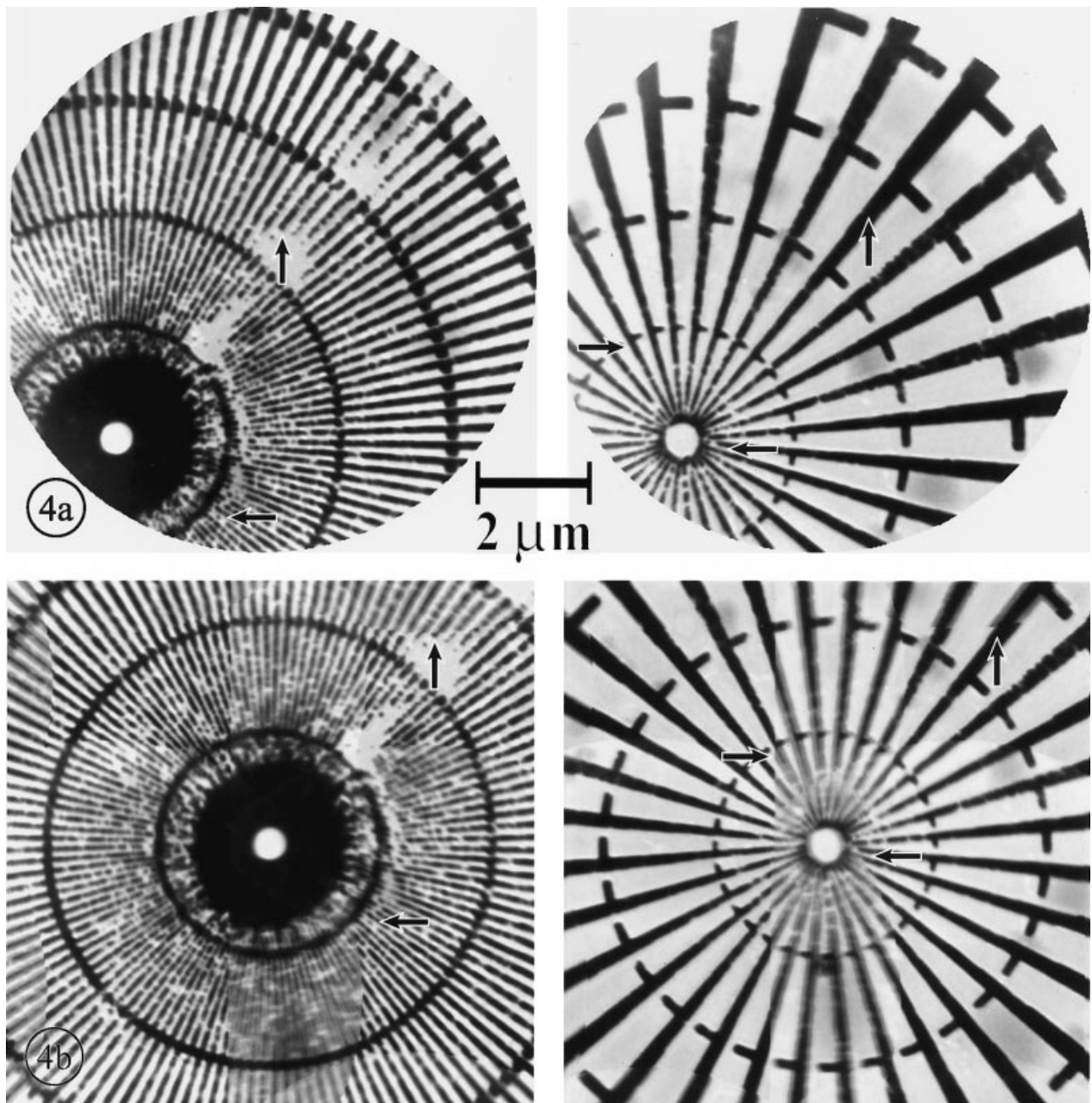
Fig. 3. (*Continued*)

Fig. 4. Performance of registration on microfabricated gold structures, with finest feature dimensions of about 40 nm. a, Two individual high-resolution subimages from the central parts, containing the finest features, of each of the structures. Such images have been used to measure the resolution of the microscope, determined to be 43 nm. The pixel size is 20 nm. b, Corresponding parts of the montage assembled using only the recorded stage positions, without registration by cross-correlation. The stage position determination errors are sufficient to degrade the resolution significantly. Arrows indicate some fine features in overlap regions that are blurred due to misregistration. c, The full montage of both gold structures, registered using the montage assembly algorithm. It spans an area of about $104 \times 94\,\mu$m (5200×4700 pixels at 20 nm pixel size). Inset images show the same central areas. Full resolution is preserved when compared to the individual subimages (a), which demonstrates essentially perfect registration.
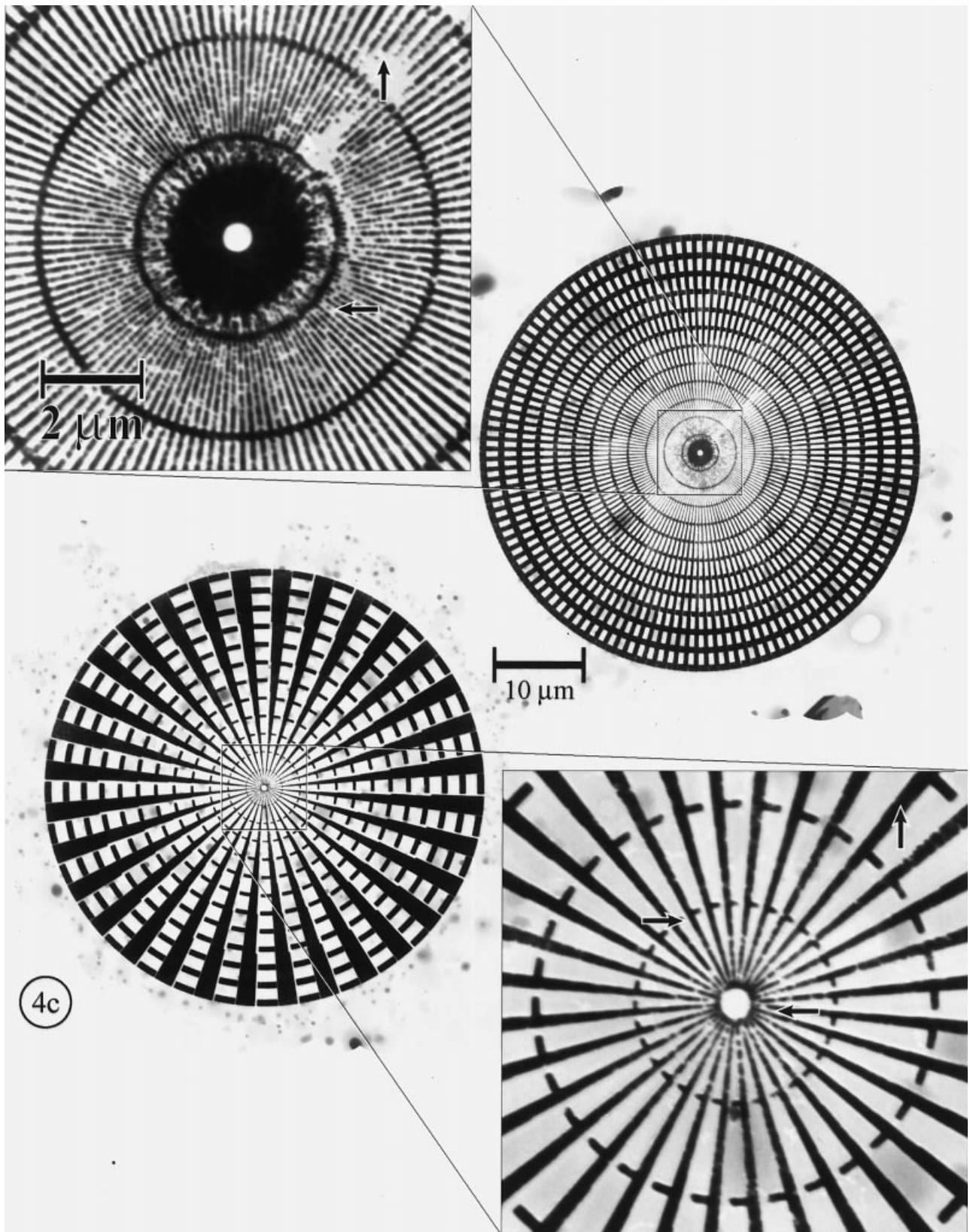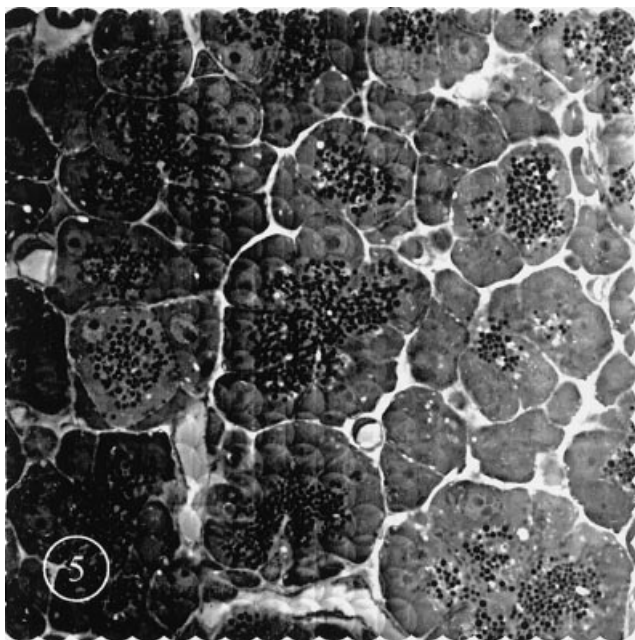
Fig. 4. (*Continued*)

Fig. 5. Effect of time varying pattern of illumination. The pattern of illumination changes gradually with time, due to drift of either the synchrotron source or microscope optics. In this montage of pancreatic tissue, 400 subimages, collected over about 3 h, are each normalized to background images acquired just before the beginning of the sequence (starting at the upper right corner). This results in a significant intensity gradient across the montage, and mismatched intensities at subimage borders. When each subimage is normalized to a time interpolated background image, constructed from multiple background images acquired throughout the sequence, a proper correction is obtained (see Fig. 7).

specified subimage, or the centremost one by default. Registering subimages with extracted target regions of the developing montage also affords certain advantages. First, it is more robust, because any neighbours of a particular subimage that have already been inserted contribute to its reference image, increasing the amount of feature overlap. It is also more computationally efficient because registration is performed on each subimage only once. Moreover, the approximate insertion position and the maximum shift are already known from the stage position, reducing the search space, and therefore computation. An optimization similar to the latter is achieved in some other published algorithms using a multi-resolution pyramid approach (Dani & Chaudhuri, 1995; Vogt *et al.*, 1996). However, these still require pairwise cross-correlation operations between each subimage and multiple neighbours.

As for the registration step itself, many methods have been devised for mutually aligning images (e.g. Brown, 1992). Ours can be considered a hybrid of the two main approaches, i.e. signal processing/statistical analysis and computer vision/image understanding. The first is represented by generalized correlation methods, in particular maximum

likelihood estimation (Knapp & Carter, 1976; Eversole & Nasburg, 1983). This method can be thought of (Knapp & Carter, 1976) as filtered cross-correlation in which two filters are applied. One is a whitening filter to deconvolve the signal autocorrelation from the delta function representing the image shift, and is generally high pass in nature for real-world images (Pratt, 1974). The other is a SNR filter to suppress frequencies with high noise power, and is generally low pass in nature. Overall, the combined filters have bandpass characteristics. The statistical nature of the signal and noise components of the images must be known, estimated, or assumed in order to determine the exact filter weights. Instead of attempting to estimate optimal filter parameters, we have simply chosen a generic bandpass filter (the difference of Gaussians) that we have found to work well on our images. In addition, the derivation of the optimal estimate generally assumes a large region of overlap between the signals or images. However, when assembling montages in microscopy, an attempt is generally made to overlap the subimage fields by a narrow margin, especially when minimal sample exposure is desired, as in fluorescence microscopy because of bleaching, and electron and X-ray microscopies because of radiation damage. In this case, the intersection between the regions of support of the search and reference images changes substantially with displacement, producing a slowly varying intensity background in the correlation image that can overwhelm the true peak (see Fig. 2). Here, filtering with the difference of Gaussians, which tapers to zero weight at zero frequency, has the additional advantage that it suppresses this low frequency intensity background.

The second approach consists of a wide variety of non-linear operations that are designed to extract features from the images to be registered. The correspondence between these features can then be determined. For example, Turner *et al.* (1997) identify specific landmarks such as cell nuclei in the subimages by image segmentation, and register corresponding ones. This approach can give highly accurate registration. However, it requires that the segmented features be well distributed in the regions of overlap between subimages. In addition, segmentation algorithms tend not to be generalizable to all kinds of sample. We have found that the gradient magnitude operator, a step down from true image segmentation, is a simple, general, and reliable means of emphasizing features for registration in images. Although it might be expected to perform poorly in the presence of noise due to its high pass nature, this does not seem to be a problem even when noise levels are much higher than we have observed (see Fig. 2c).

There are weaknesses common to many montage assembly algorithms, including the one described here. If for some reason one of the subimages is incorrectly registered, it can affect the positioning in the montage of subsequently inserted subimages. This can happen under

certain unfavourable conditions, for example if the area of overlap between a subimage and previously inserted subimages is relatively featureless, or contains only features that are periodic or have parallel edges. In such cases the
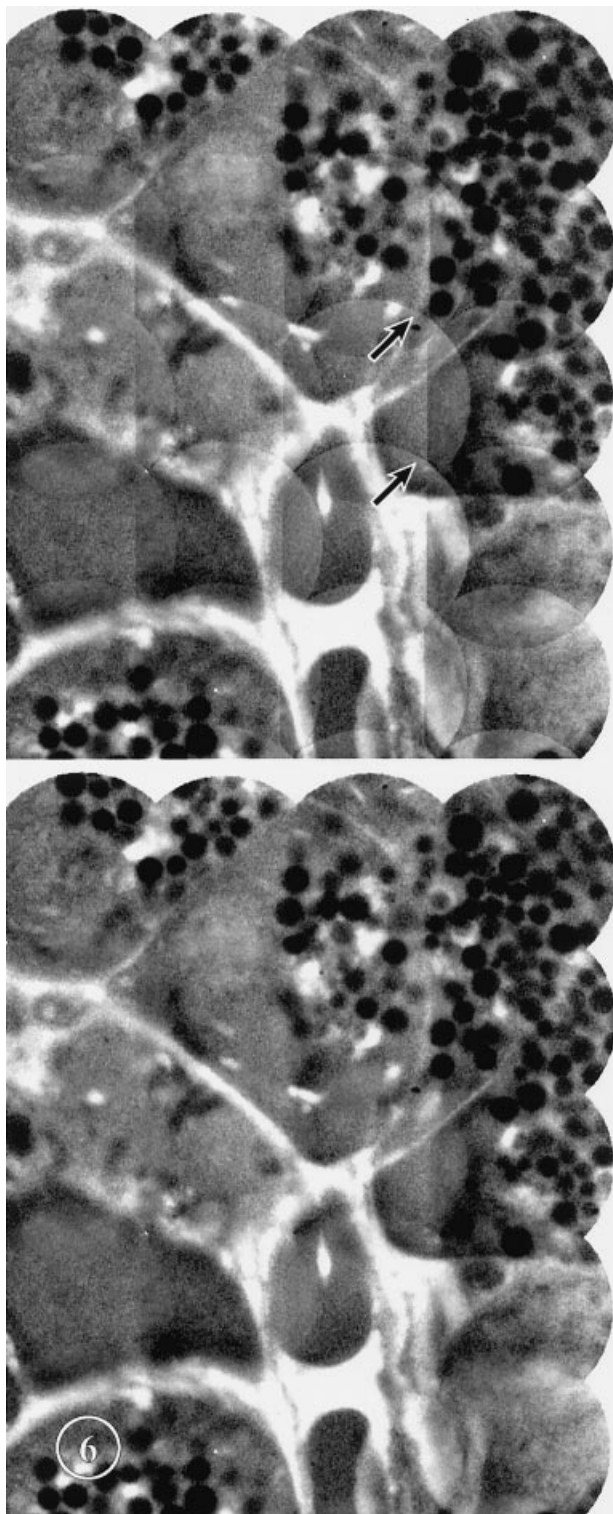
cross-correlation would have an ambiguous or non-unique peak. Alternatively, features in the overlapping areas might change between exposures. Exposure-induced changes in the sample are frequently seen in biological electron microscopy. They can also be seen with certain samples in the X-ray microscope, particularly hydrated biological samples, although we have not noticed it in the samples we have used. This problem is complicated and might be addressed by applying some kind of warping transform designed to compensate for beam-induced artefact.

The first problem, accumulated errors due to ambiguous registration, appears more tractable however. Although the optimum registration may be ambiguous between a subimage and previously inserted subimages, it might be better between it and later subimages. Thus, one solution might be to optimize the insertion order further by dynamic reordering. If, during the registration step, the cross-correlation peak for a subimage is smaller than some significance threshold, such as a certain number of standard deviations above the mean value of the cross-correlation image, the subimage can be moved to a later position in the insertion list, such as in the next generation of neighbours. Then by the time it is inserted, more of its neighbours will have contributed to its target area in the montage, increasing the chance of an unambiguous match. Another strategy, at somewhat increased computational expense, might be to perform global optimization of registration across all the subimages. In this scheme, pairwise cross-correlations would be precomputed between all neighbouring subimages. The positions of all the subimages would then be shifted simultaneously so as to maximize the sum of all the cross-correlations, possibly by an iterative algorithm. In this way, the shift applied to any subimage would be most strongly influenced by its position relative to the neighbouring subimages with which it shares the most features, regardless of the order of insertion. A similar idea is described by Davis (1998).

An unexpected realization of montage assembly was that the method could be used to calibrate microscopes. Indeed, this may well be one of the most sensitive means available to detect small errors in magnification, rotational misalignment between the detector and sample stage, and sample stage skew. Finally, automating some of the last remaining

Fig. 6. Blending. When subimages are inserted into the montage, the areas of overlap are constructed by averaging pixel values from the contributing subimages (top). Despite the corrections that have been applied, some residual uncorrected factor, possibly scattered light, sometimes causes an intensity mismatch at the subimage borders (arrows). Blending can be performed (bottom) by using a weighted average in the overlapping areas, with weights that taper near the subimage borders. The result is seamless, which facilitates subsequent image analysis.

steps still requiring human interaction, such as background region selection, blemish identification in background images, initial exposure selection, and subimage region of support masking, can be accomplished entirely in software, and would involve relatively simple computer vision algorithms. Automatic sample focusing (in the VLM) could also be implemented, and would require the addition of a motorized VLM focusing stage.
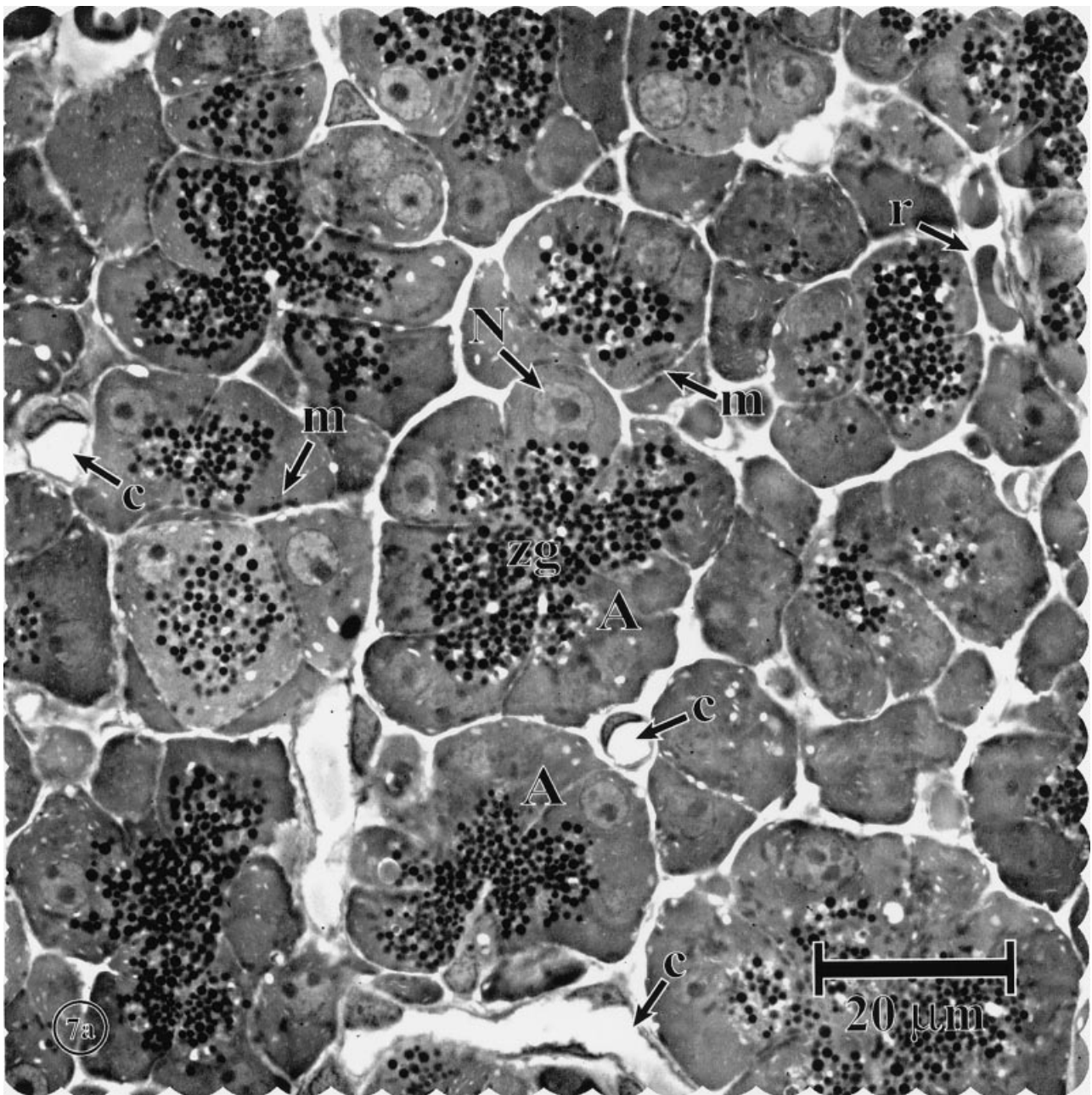

Fig. 7. High-resolution, large-field montage of a pancreatic tissue section. a, The full montage of 400 subimages, spanning $110 \times 110 \, \mu$m (about 2700×2700 pixels at 40 nm pixel size). The exocrine (acinar) cells of the pancreas are arranged in clusters called acini (A). Throughout the tissue are capillaries (c), some of which are sectioned at the level of the capillary endothelial cell nucleus. Red blood cells (r) are also seen. Several intracellular organelles are demonstrated in this view, including cell nuclei (N), mitochondria (m) and numerous dense, round zymogen granules (zg) that store digestive enzymes prior to their secretion into the gut, clustered at the apical end of the acinar cells. b, Full resolution view of the acinus in the centre of a. Again the nucleus (N), nucleolus (n), mitochondrion (m) and zymogen granule (z) are demonstrated, but now in more detail. Patterns of fine linear lucencies are also visible in the basolateral region of some cells. These may represent endoplasmic reticulum cisternae that are orientated perpendicular to the plane of sectioning (er).
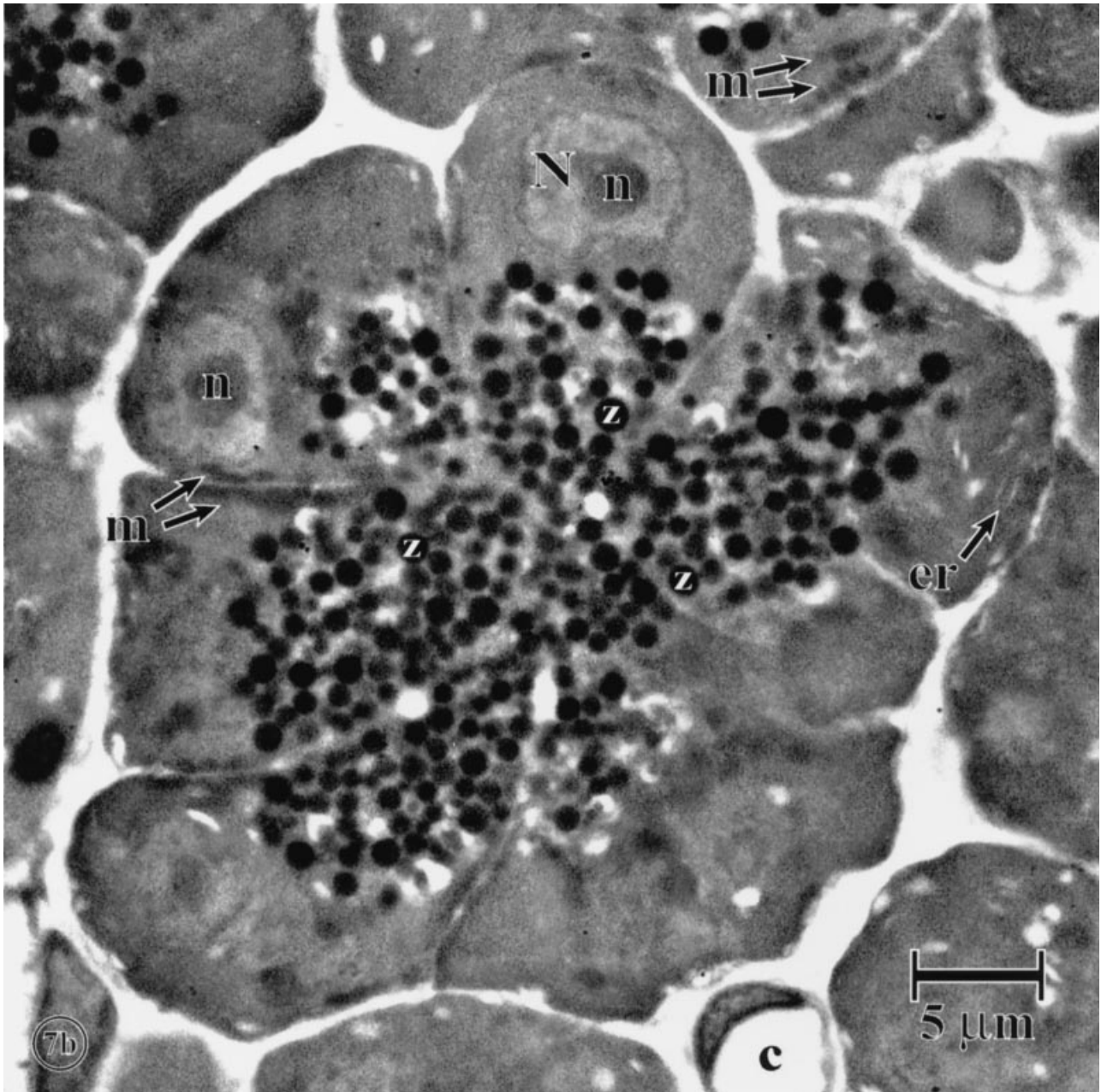
Fig. 7. (*Continued*)

The major accomplishments of this work, in addition to the high quality images that were produced, were the methods we adapted and developed to obtain photometrically accurate X-ray images that allow quantitative measurements of cellular structures, and to explore large fields of view at the maximum resolution of the microscope. These capabilities were indispensable for the studies we hoped to undertake. In particular, we planned to make quantitative estimates, the first of their kind, of the protein mass of individual zymogen granules *in situ*, to establish how that mass varies among these objects, and to extrapolate such measurements, as well as parameters such as size and number, to the population as a whole. Aside from its particular biological interest, such a capability would illustrate the utility of X-ray microscopy for ultrastructural research, particularly when there is a desire to obtain quantitative information about the chemical contents of an object. The use of automation and montage assembly techniques makes it possible to overcome a major shortcoming of X-ray microscopy as a practical tool

for biological research to this point – the inability to examine a sample of sufficient size to provide fully realized generalizations about the material under study.

Acknowledgements

We would like to dedicate this paper to the memory of our friend, colleague, and co-author, Werner Meyer-Ilse (1954–1999). Dr Meyer-Ilse was the principal scientist responsible for the development of the XM-1 transmission soft X-ray microscope at Lawrence Berkeley National Laboratory used in this study. The microscope was his passion, and he was intimately involved in every aspect of its design, implementation, operation, and maintenance. He died on 14 July 1999 from injuries sustained in an automobile accident while visiting his native Germany. Werner had a rare combination of integrity, charity, brilliance, and professionalism, and he will be sorely missed.

References

Anderson, E.H. & Kern, D. (1992) Nanofabrication of zone plates for X-ray microscopy. *X-Ray Microscopy III: Proceedings of the Third International Conference, London, September 3–7, 1990* (ed. by A. G. Michette, G. R. Morrison and C. J. Buckley), pp. 75–78. Springer-Verlag, Berlin.

Azaria, M. & Hertz, D. (1984) Time delay estimation by generalized cross correlation methods. *IEEE Transactions on Acoustics, Speech and Signal Processing*, **ASSP-32**, 280–285.

Brown, L.G. (1992) A survey of image registration techniques. *ACM Computing Surveys*, **24**, 325–376.

Dani, P. & Chaudhuri, S. (1995) Automated assembling of images: image montage preparation. *Pattern Recognition*, **28**, 431–445.

Davis, J. (1998) Mosaics of scenes with moving objects. *Proceedings of the 1998 IEEE Computer Society Conference on Computer Vision and Pattern Recognition, Santa Barbara, California*, pp. 354–360. IEEE Computer Society, Los Alamitos.

Dereniak, E.L. & Crowe, D.G. (1984). *Optical Radiation Detectors*. John Wiley & Sons, New York.

Eversole, W.L. & Nasburg, R.E. (1983) Maximum likelihood estimation for image registration. *Applications of Digital Image Processing VI, San Diego, California, August 23–26, 1983* (ed. by A. G. Tescher), pp. 190–194. Proceedings SPIE, Vol. 432.

Heck, J.M., Attwood, D.T., Meyer-Ilse, W. & Anderson, E.H. (1999) Resolution determination in x-ray microscopy: an analysis of the effects of partial coherence and illumination spectrum. *J. X-Ray Sci. Technol.* **8**, 95–104.

Henke, B.L., Gullikson, E.M. & Davis, J.C. (1993) X–ray interactions: photoabsorption, scattering, transmission, and reflection at E = 50–30000 eV, Z = 1–92. *Atomic Data Nuclear Data Tables*. **54**, 181–342.

Kirz, J., Jacobsen, C. & Howells, M. (1995) Soft X-ray microscopes and their biological applications. *Q. Rev. Biophys.* **28**, 33–130.

Knapp, C.H. & Carter, G.C. (1976) The generalized correlation method for estimation of time delay. *IEEE Transactions on Acoustics, Speech and Signal Processing*, **ASSP-24**, 320–327.

Krivanek, O.L. & Mooney, P.E. (1993) Applications of slow-scan CCD cameras in transmission electron microscopy. *Ultramicroscopy.* **49**, 95–108.

Loo, B.W. Jr, Parvin, B. & Rothman, S.S. (1996) Two- and three-dimensional segmentation for measurement of particles in the analysis of microscopic digital images of biological samples. *Three-Dimensional Microscopy: Image Acquisition and Processing III, San Jose, California, January 30–February 1, 1996* (ed. by C. J. Cogswell, G. S. Kino and T. Wilson), pp. 209–215. Proceedings SPIE, Vol. 2655.

Meyer-Ilse, W., Medecki, H., Brown, J.T., Heck, J.M., Anderson, E.H., Stead, A., Ford, T., Balhorn, R., Petersen, C., Magowan, C. & Attwood, D.T. (1998) X-ray microscopy in Berkeley. *X-Ray Microscopy and Spectromicroscopy: Proceedings of the Fifth International Conference, Würzburg, August 19–23, 1996* (ed. by J. Thieme, G. Schmahl, D. Rudolph and E. Umbach), pp. I-1–I-12. Springer, Berlin.

Meyer-Ilse, W., Medecki, H., Jochum, L., Anderson, E., Attwood, D., Magowan, C., Balhorn, R., Moronne, M., Rudolph, D. & Schmahl, G. (1995) New high-resolution zone-plate microscope at Beamline 6.1 of the ALS. *Synchrotron Radiation News*, **8**, 29–33.

Pratt, W.K. (1974) Correlation techniques of image registration. *IEEE Transactions on Aerospace and Electronic Systems*, **AES-10**, 353–358.

Rothman, S., Anderson, E., Attwood, D., Batson, P., Buckley, C., Goncz, K., Howells, M., Jacobsen, C., Kern, D., Kirz, J., Rarback, H., Rivers, M., Shu, D., Tackaberry, R. & Turek, S. (1990) Soft x-ray microscopy in biology and medicine: status and prospects. *Physica Scripta*, **T31**, 18–22.

Rothman, S.S., Goncz, K.K. & Loo, B.W. Jr (1992) Following protein transport with the high resolution x-ray microscope. *X-Ray Microscopy III: Proceedings of the Third International Conference, London, September 3–7, 1990* (ed. by A. G. Michette, G. R. Morrison and C. J. Buckley), pp. 373–383. Springer-Verlag, Berlin.

Schmahl, G., Rudolph, D., Niemann, B. & Christ, O. (1980) Zone-plate x-ray microscopy. *Q Rev. Biophys.* **13**, 297–315.

Schmahl, G., Rudolph, D., Schneider, G., Thieme, J., Schliebe, T., Kaulich, B. & Hettwer, M. (1996) Diffraction optics for X-ray imaging. *Microelectron. Eng.* **32**, 351–367.

Thieme, J., Schmahl, G., Rudolph, D. & Umbach, E. (eds) (1998) *X-ray Microscopy and Spectromicroscopy: Proceedings of the Fifth International Conference, Würzburg, August 19–23, 1996.* Springer, Berlin.

Turner, J.N., Ancin, H., Becker, D.E., Szarowski, D.H., Holmes, M., O'Connor, N., Wang, M., Holmes, T. & Roysam, B. (1997) Automated image analysis technologies for biological 3D light microscopy. *Int J. Imag. Syst. Technol.* **8**, 240–254.

Vogt, R.C., Trenkle, J.M. & Harmon, L.A. (1996) Mosaic construction, processing, and review of very large electron micrograph composites. *Applications of Digital Image Processing XIX, Denver, Colorado, August 7–9, 1996* (ed. by A. G. Tescher), pp. 2–15. Proceedings SPIE, Vol. 2847.

Wilhein, T., Rothweiler, D., Tusche, A., Scholze, F. & Meyer-Ilse, W. (1994) Thinned, back-illuminated CCDs for x-ray microscopy. *X-Ray Microscopy IV: Proceedings of the Fourth International Conference, Chernogolovka, Russia, September 20–24, 1993* (ed. by V. V. Aristov and A. I. Erko), pp. 470–474. Bogorodskii Pechatnik, Chernogolovka.